Ultrahigh optical Q factors of crystalline resonators in the linear regime

Ivan S. Grudinin, Vladimir S. Ilchenko, and Lute Maleki*
Jet Propulsion Laboratory, California Institute of Technology, Pasadena, California 91109 USA†
(Received 2 June 2006; published 8 December 2006)

Experimental demonstration of record optical quality factor of $(6.3\pm0.8)\times10^{10}$ corresponding to cavity ring-down time of $\tau\simeq36$ μs is made possible by avoiding nonlinear effects in a crystalline whispering gallery mode resonator. We discuss various loss mechanisms in CaF_2 cavities and ways of achieving higher quality factors. Possible applications in quantum optics and photonics are discussed.

DOI: 10.1103/PhysRevA.74.063806 PACS number(s): 42.60.Da, 42.65.−k, 42.50.Pq

I. INTRODUCTION

Whispering gallery mode (WGM) resonators have been receiving increasing attention as novel structures with unique features suitable for various applications in linear, nonlinear, and quantum optics [1–3]. In particular, a combination of a small mode volume and a high optical quality factor (Q) is a unique feature of these resonators that makes it possible to achieve high concentration of the optical field and relatively long photon confinement times. These dielectric cavities have no mirrors—light is trapped by total internal reflection at a dielectric boundary. The optical quality factor is one of the most important characteristics of the WGM resonator. It is directly related to the cavity ringdown time $\tau=Q/\omega$. In a cavity with radius a and refractive index n, the resonant increase of the effective intracavity intensity I_c over the input light intensity I at a free space wavelength λ is proportional to the Q factor: $I_c/I_0=Q\lambda/(\pi^2 na)$. Long storage times or long effective optical path lengths are important for efficient nonlinear interactions and for cavity quantum electrodynamics (CQED) experiments. Recently, it has been shown that extreme material purity and higher nonlinearities of crystalline resonators may provide improved photon confinement times [4], enhanced second harmonic generation [5], and low threshold hyperparametric oscillations [6] in WGMR.

The interest in ultra-high quality factors in support of new applications of WGM resonators requires new strategies for the fabrication and characterization of the resonators. The Q factor, for example, is commonly measured using either cavity ringdown or linewidth calibration techniques. The presence of strong nonlinear processes, though, makes it difficult to properly determine the Q with these traditional techniques. The nonlinear processes include thermal and Kerr nonlinearities, stimulated Raman scattering and thermo-optical instability, all of which can influence an accurate determination of the intrinsic Q.

The purpose of the present work is to study the ultimate limit of the Q of the crystalline resonators, and describe techniques for measuring ultra-high values. The outline of the paper is as follows. The crystalline WGM resonator fabrication technique is briefly discussed followed by the results of Q factor measurements at three wavelengths, including a new record value for the quality factor of a WGM resonator. We also demonstrate the difference in cavity resonance curves obtained at different pump power levels. In the next section we analyze loss mechanisms that limit the Q factor of crystalline cavities and give estimates for CaF_2 resonators. In the section on the nonlinear processes, we discuss the influence they have on the shape of a resonant curve. The thresholds for Raman lasing, thermo-optical oscillations, thermal and Kerr bistabilities are also discussed. We show that it is only possible to measure ultra high Q in the linear regime by lowering the optical power. In the final section we discuss the role of impurities and means for achieving higher optical Q factors in crystalline cavities, together with some potential applications.

II. MEASUREMENT OF OPTICAL Q FACTOR OF CRYSTALLINE WGM RESONATORS

A. Fabrication of the cavities

Crystalline WGM resonators were fabricated with a novel technique developed in our laboratory. A small cylinder is first cut out of a crystalline blank. The axis of the cylinder coincides with the blank axis, which is along [111] crystalline orientation. This cylinder is mounted onto an air bearing spindle of a home-made diamond turning apparatus. Diamond cutting of a desired profile is performed with a precise computer controlled lathe. This step produces resonators with optical Q factors of about 10^7. The next step involves hand polishing with a sequence of diamond abrasives of decreasing grit sizes. A thorough cleaning procedure is performed after each polishing step. An example of a resonator is shown in Fig. 1. This fabrication technique is applicable to many optical crystals due to the versatility of the diamond grinding process. Resonators may be fabricated with any diameter down to a few tens of microns [7]. Moreover, many resonators may be fabricated on the same rod with small separations. The resulting resonator chains may be utilized in filtering and other applications and are similar to coupled pendulums in mechanics [8]. A chain of three CaF_2 cavities presented on Fig. 2 was fabricated in our lab. The resonators are separated by 70 μm and show resonant coupling.

B. Measurement of a Q factor

We have measured the optical Q factor of CaF_2 resonators at laser wavelengths of 1064 and 1550 nm using direct ob-

*Electronic address: grudinin@caltech.edu
†URL: http://horology.jpl.nasa.gov/quantum/

FIG. 1. (Color online) CaF_2 cavity with a record Q factor of $(6.3\pm0.8)\times10^{10}$, 5.5 mm in diameter. White brackets show the area of WGM localization.

servation of cavity resonances. Measurements were also performed at 780 nm using a "self-homodyne method" (Fig. 3). Noise from our 780 nm grating stabilized diode laser made it impossible to resolve the resonance curve directly. In a "self-homodyne" method, Q factor is derived from the decay time of the interference pattern formed by two beams. The first is the laser beam with its optical frequency linearly dependent on time and the second beam is the cavity emission. As the laser frequency is scanned, at some point it excites a cavity mode and stores some energy in it. This energy will then be emitted into the coupling element as a single frequency exponentially decaying optical beam. Interference of this beam with the laser beam results in exponentially decaying oscillations, from which a decay time may be extracted and the Q factor computed according to $Q=\omega T/2$ (Fig. 3).

In order to achieve the flexibility to use various wavelengths of light, we utilized a conventional prism coupler to excite the modes of the cavity. The critical coupling efficiency was above 30 percent at all wavelengths. All measurements were performed in a strongly undercoupled regime where only a small fraction of light enters the cavity, leaving the measured Q factor close to the intrinsic value.

The 1064 nm Lightwave Nd:YAG and 1550 nm Coheras Adjustik lasers have narrow line of a few kilohertz, which made it possible to use direct observations of cavity resonances. Laser frequency was modulated with an internal piezo actuator. Signal generators were used to feed the sum of two signals to the laser head. The first is a sawtooth-shaped voltage for scanning the frequency back and forth over the cavity resonance. The second is a weak sinusoidal signal at 100 kHz for sideband modulation of the laser carrier. Sideband modulation provides calibration peaks shifted by 100 kHz both ways around the cavity resonance frequency. These peaks were recorded simultaneously with the cavity resonance curve and used for frequency calibration. A direct high frequency modulation of the laser carrier through an internal piezo element results in a weak amplitude modulation. This amplitude modulation was rejected by the detector with a large response time. Example of the Q factor measured with this method is shown on Fig. 4. The best value measured at 1550 nm was $Q=1.1\times10^{10}$. The quality factor was also measured for a 1.5 mm CaF_2 cavity at 1064 nm and

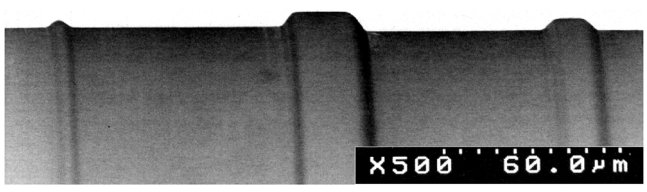

FIG. 2. Evanescent-field coupled CaF_2 WGM resonators. The rod diameter is 5 mm and the electron microscope is focused to the side of the rod to make the shape of the resonators visible. The resonator on the left supports only one mode per free spectral range [9].

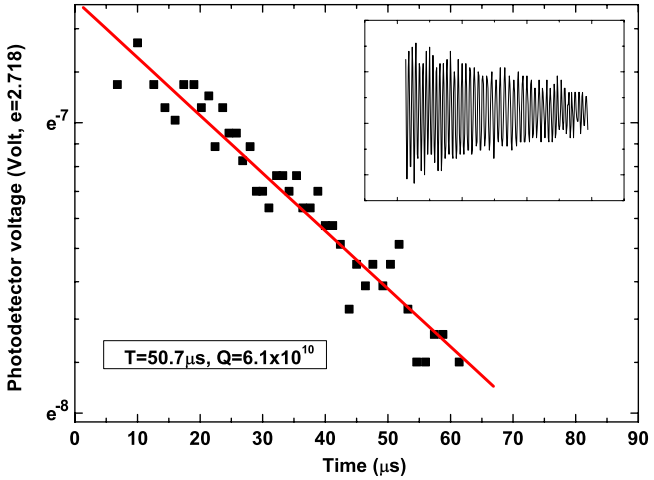

FIG. 3. (Color online) Example of "self-homodyne" measurement of ringdown time at 780 nm at low power. The inset shows the exponentially decaying oscillations resulting from the interference of the laser beam and the cavity emission.

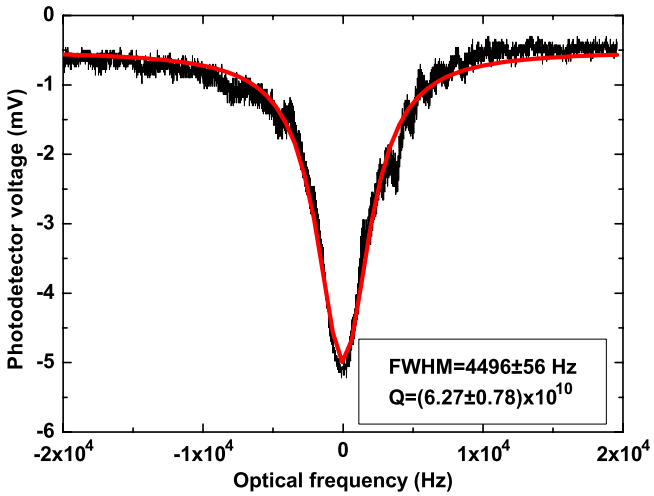

FIG. 4. (Color online) CaF_2 cavity resonance showing record optical Q factor and a Lorentzian fit. Measured at a coupled pump power of 100 nW in a strongly undercoupled regime. Out of resonance photodetector level is −0.5 mV.

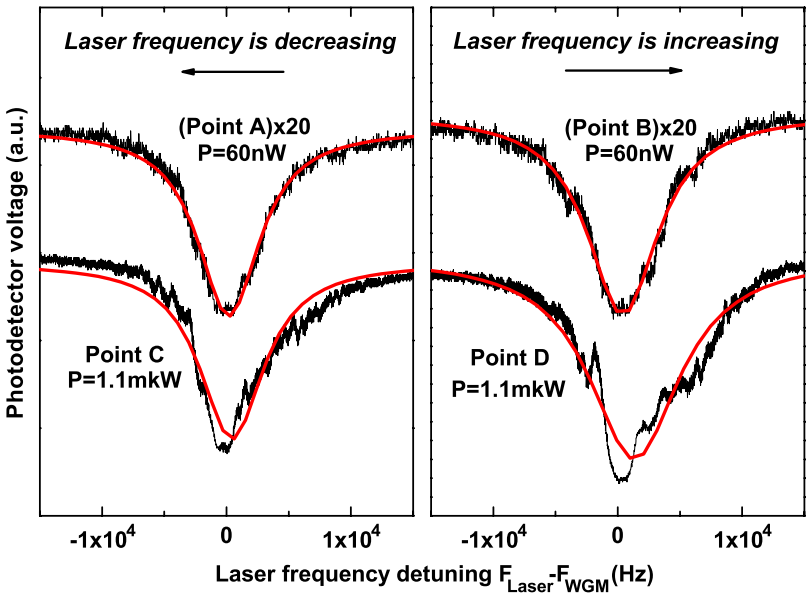

FIG. 5. (Color online) Cavity resonances recorded at pump power $P \simeq 60$ nW and $P \simeq 1$ μW. Red traces show Lorentzian fit. It can be seen that the resonance curves are not Lorentzian for higher values of the input power.

found to be 4×10^{10}. In a fluoride microresonator 100 μm in diameter values as high as $Q=4 \times 10^8$ were found to be achievable for a UV-grade material at 1064 nm. The free spectral range of our cavities comprises many WGM's and the process of measurement included a search for the modes with the highest values of Q.

C. Q factor and pump power

In order to observe the influence of the input optical power that was used to excite the WGM's on the effective Q factor, we performed a series of measurements for a selected cavity mode. Measurements were performed for coupled pump power levels ranging from a few nanowatt to a microwatt. For each power level the laser was swept over the cavity resonance twice, first as its frequency was decreasing and second as it was increasing. This produced two resonant curves for each pump power level. Quality factors were obtained by fitting the cavity response curves to a Lorentzian for both laser frequency scan directions. We fit the dependence of the quality factor on power to exponentials for illustration—to delineate the data points. These exponentials converge to a single value of Q for low optical power, as expected. It should be noted that the intrinsic Q factor of a cavity generally should not depend on the optical excitation power. The observed divergence is generated by the method used to derive the Q factors. Figure 5 serves to clarify this statement. It represents four measurements of the same WGM at coupled pump powers of 60 nanowatt and 1 microwatt. These measurements correspond to points A,B,C,D in the Fig. 6. For the upper trace the pump power is well below the threshold of nonlinearities and the resonant curve is Lorentzian. For the lower trace the higher pump power causes the curves to deviate from the Lorentzian shape and become nonsymmetric. The asymmetry arises from thermal nonlinearity, which in our case causes the cavity eigenfrequency to decrease as the laser beam begins to

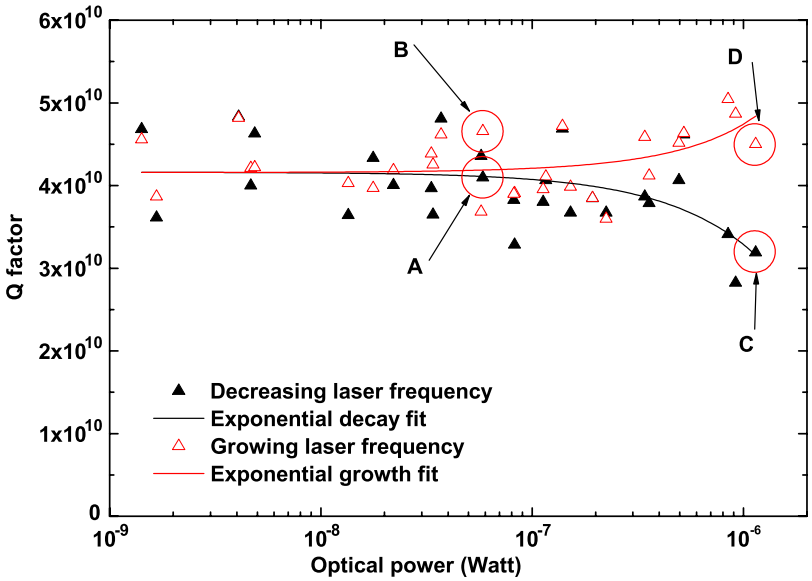

FIG. 6. (Color online) The quality factor measured by fitting the cavity response curve to a Lorentzian for several pump power levels. Measurements at points A,B,C,D were used to build the Fig. 5.

heat up the cavity material. As will be discussed in the following sections, measurements A and B correspond to a power level that is below the Raman lasing threshold, and thresholds of other nonlinear effects. For these measurements one may observe the linear oscillator response independent of the direction of the frequency scan and thus be able to obtain a reliable estimate for the cavity's intrinsic Q factor. Occasional deviations from a Lorentzian were still observed due to the acoustic noise perturbations and the high pass filter in the AC-coupled input of the oscilloscope.

III. LOSSES IN CRYSTALLINE CAVITIES

Given the Beer-Lambert law for light absorption $I(x)=I_0e^{-\alpha x}$, which holds when the nonlinear optical processes are not present, the maximum value of the optical Q factor of a dielectric WGM resonator is given by

$$Q_{\max}=\frac{2\pi n}{\lambda\alpha}. \tag{1}$$

Here α is a total optical loss coefficient in nepers per meter, which is a measure of the cumulative attenuation caused by different mechanisms:

$$\alpha=\alpha_{ss}+\alpha_{mat}+\alpha_{coupling}+\alpha_{rad.} \tag{2}$$

The contributions from several loss mechanisms are added: surface scattering, material losses, influence of the coupler, and the radiative loss. Surface scattering is induced by the imperfections of the surface. Material losses are caused by the fundamental absorption in the material, atomic impurities and three types of bulk scattering: Raman, Brillouin, and Rayleigh. Radiative loss is only significant in small microresonators. The coupler losses can be made small by performing measurements in a strongly undercoupled regime.

A. Surface scattering

Surface roughness may be induced by frozen capillary waves, as in the case of the fused silica resonators, or by imperfections of polishing, in the case of crystalline resonators. In addition, some amount of micro- and nano-particles is almost always present on the surface of a resonator. For estimating the surface-limited Q factor, one approach uses parameters of surface roughness σ and correlation length B [10],

$$Q_{ss}=\frac{K_{TE,TM}}{(K_{TE,TM}+1)}\frac{3\lambda^3 a}{8n\pi^2B^2\sigma^2}. \tag{3}$$

Here $K_{TE}=2.8$, $K_{TM}=9.6$ are scattering suppression coefficients for TE and TM whispering gallery modes in fused silica. Since the refractive index of fused silica $n=1.45$ is close to that of CaF_2, $n=1.43$ we shall use fused silica suppression coefficients for our estimates. The formula was obtained as an approximation which takes the correlation length to be much smaller than the wavelength of light ($\sigma B^2 \ll \lambda^3$). We may use this equation to analyze the atomic force microscope (AFM) images of CaF_2 resonators taken in the WGM localization area (Fig. 7). Since noise due to the AFM and that of the surface roughness are independent, the variance of the image data is a sum of the surface and noise variances $\sigma^2_{image}=\sigma^2_{surface}+\sigma^2_{noise}$. Given the AFM empty image (noise) standard deviation of $\sigma_{noise}=0.07$ nm we calculate surface roughness σ for the left and right image to be 0.186 nm and 0.151 nm, correspondingly. Calculations were made with a standard expression for the unbiased variance. These values are significantly smaller than those typical of fused silica resonators [11], and demonstrates the capability of our fabrication technique. It is possible to achieve even better results if advanced polishing techniques are used. In order to use the analysis, the correlation length B should also be computed. The correlation length is defined as the decay length of the exponential autocorrelation function. We are interested in the correlation length along the direction of light propagation, which in our case is coincident with the direction of polishing traces. Computer algorithms of the image rotation generally alter the correlation function. In addition, the autocorrelation function depends on the direction of computation for our type of the surface. In order to overcome these problems, a two-dimensional correlation function may be computed with the use of a Wiener-Khinchin theorem and fast Fourier transform algorithms. Computed autocorrelations can be seen in Fig. 7 below the surface scans and are represented as levels in white. The black color corresponds to the zero level. Since polishing leaves some traces as can be seen on Fig. 7, the two-dimensional autocorrelation functions decay slowly in the direction of polishing, masking short range surface structures in this direction. We may use the correlation length measured in the direction orthogonal to polishing traces to obtain the characteristic radius of the surface features. Such an approach is justified as the shape of the scatterer is irrelevant [12]. For both images this gives $B\simeq 40$ nm. These computed parameters give $Q_a=4.3\times10^{11}$ and $Q_b=6.6\times10^{11}$ for surface limited Q factors.

A number of inclusions with diameters of 30–50 nm protrude from the surface by only about 1–2 nm, and can be seen in Fig. 7. These inclusions could possibly be the "shadows" of the diamond nanoparticles used in the polishing process that were buried in the surface layer. The assumption that there are particles inside the surface is reasonable as it is known that a thin 0.1 μm surface layer may flow when the surface is being polished, thus trapping the polishing particles [13]. Particle scattering limited Q when K 50 nm diamond spheres are embedded into the surface is given by

$$Q_{sp}=\frac{2\pi n V_{lm1}}{K\lambda\sigma_{sp}},\quad \alpha_{sp}=\frac{K\sigma_{sp}}{V_{lm1}}. \tag{4}$$

Here σ_{sp} is a classical cross-section of a spherical scatterer [14]:

$$\sigma_{sp}=\frac{8\pi}{3}k^4r^6\left(\frac{\epsilon_s-\epsilon_c}{\epsilon_s+2\epsilon_c}\right)^2, \tag{5}$$

α_{sp} is a corresponding loss decrement and V_{lm1} is a WGM volume, which may be estimated as [15]

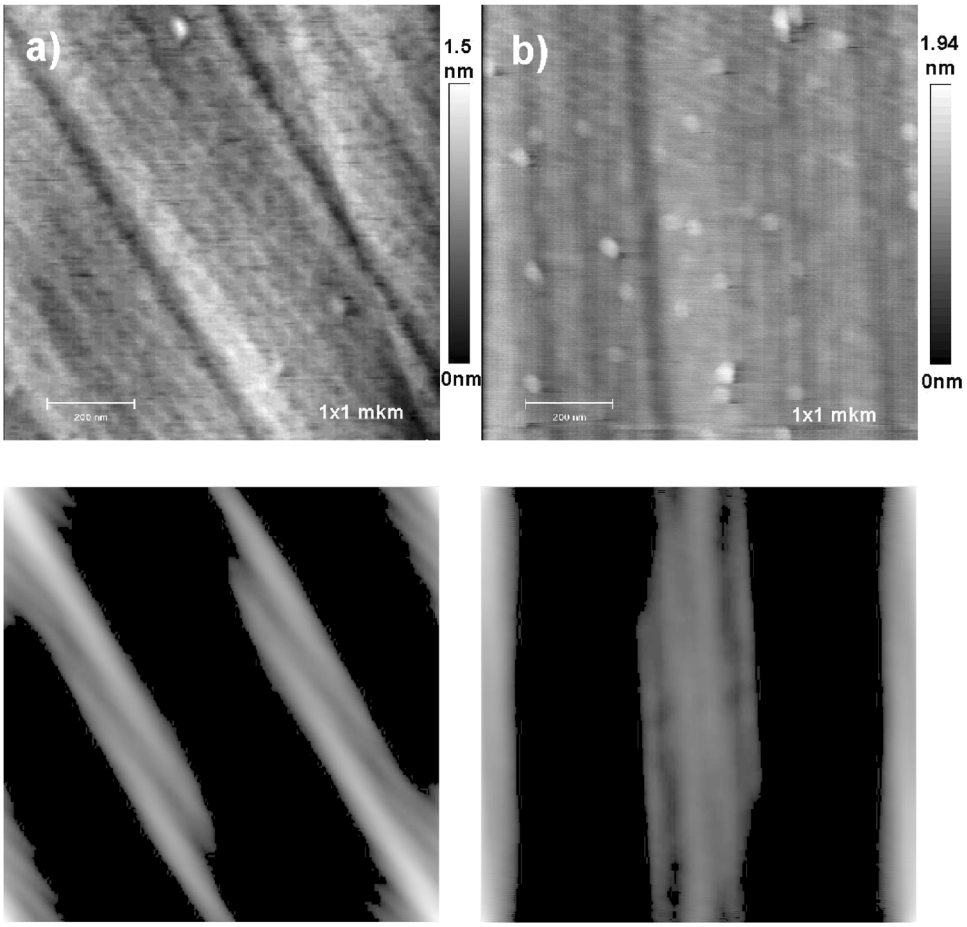

FIG. 7. AFM surface scans of two regions of WGM localization and images of corresponding two-dimensional autocorrelation functions. Squares are 1×1 micrometer.

$$V_{lm1} \simeq 3.4\pi^{3/2}\left(\frac{\lambda}{2\pi n}\right)^3 l^{11/6}\sqrt{2(l-m)+1}. \quad (6)$$

Here l and m are the mode indices, $l \simeq 2\pi an/\lambda$. This gives $Q=7\times10^{12}/\mathrm{K}$ which means that even with 100 such embedded particles a scattering limited Q of 7×10^{10} can be achieved. Unfortunately, available images cover only a minor portion of the surface area, so it is difficult to determine the actual concentration of nanoparticles on the surface of our resonators.

Another possible explanation for the observed particle-like structures in Fig. 7 might be the chemical reactions between the CaF_2 surface layer and the constituents of air. Air induced roughness of cleaved CaF_2 surface was found to be characterized by randomly distributed nanometer-sized features. These features are believed to be induced by oxygen, and remain stable after formation [16].

B. Material absorption and scattering

An ideal crystal with no impurities and defects has its window of transparency defined by the tail of multiphonon absorption on the long wavelength side and by the tail of absorption caused by electronic transitions on short wavelength side, also known as the Urbach tail. Raman, Rayleigh, and Brillouin scattering mechanisms are also present in ideal crystals. It was experimentally found, and theoretically verified, that the behavior of multiphonon and Urbach tails can be quite generally described by an exponential law. As will be discussed later, of all scattering processes, only Raman scattering plays a significant role in crystalline cavities. Thus, bulk losses in CaF_2 may be approximated by the following phenomenological expression [13,17]:

$$\alpha_{\mathrm{mat}} = \alpha_{uv}e^{\lambda_{uv}/\lambda} + \alpha_{rm}\left(\frac{\lambda_r}{\lambda}\right)^{-4} + \alpha_{ir}e^{-\lambda_{ir}/\lambda}. \quad (7)$$

Here α_{uv}, α_{ir}, λ_{uv}, and λ_{ir} are the constants obtained by fitting the experimental data for UV and IR absorption coefficients. Coefficient α_{rm} accounts for scattering suppression in the case of whispering gallery modes $\alpha_{rm}=K^{-1}_{(\mathrm{TE,TM})}\alpha_r$, where α_r is mostly Rayleigh scattering losses measured at λ_r.

Experimental data on the UV absorption for determining the parameters of the Urbach tail in CaF_2 are rather scarce. Another complication is the dependence of the parameters on temperature. Impurities may have a strong effect on the UV absorption spectra of CaF_2 [18]. The UV absorption coefficient is also known to be fluence-dependent [19]. From Fig. 8 it can be seen that as technology has advanced, CaF_2 blanks of higher purity have appeared. We assume that absorption for wavelengths longer than the UV cut-off is determined by impurities. The absorption coefficient for the cut-off wavelengths follows an exponential law. We have found that the data by Laufer *et al.* [20] may be used to estimate the parameters of the Urbach tail as they represent measurements in the UV-cut off region. Parameters of the multiphonon ab-

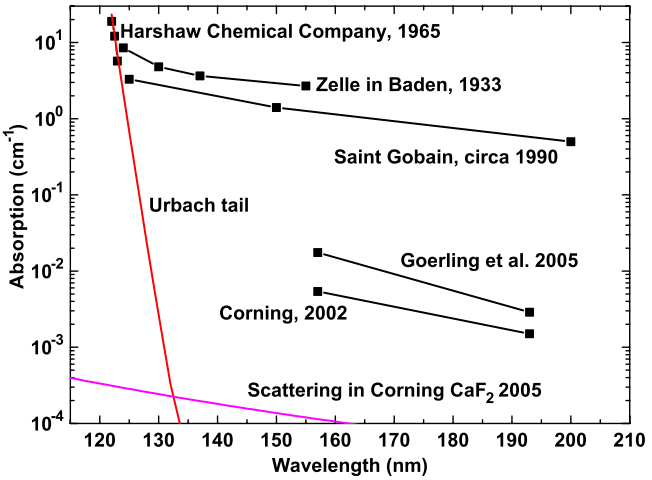

FIG. 8. (Color online) Absorption in CaF_2 and Urbach tail. Data from 1965 [20] corresponding to the three shortest wavelength points were also used to estimate the Urbach tail parameters. The 1933 data is from [21]. Saint Gobain and Corning data were obtained from the websites of those manufacturers. The scattering data was derived from [22]. Measurements by Goerling [19] are the first to separate the coefficients of bulk and surface absorption. Lines connect the data from the same source.

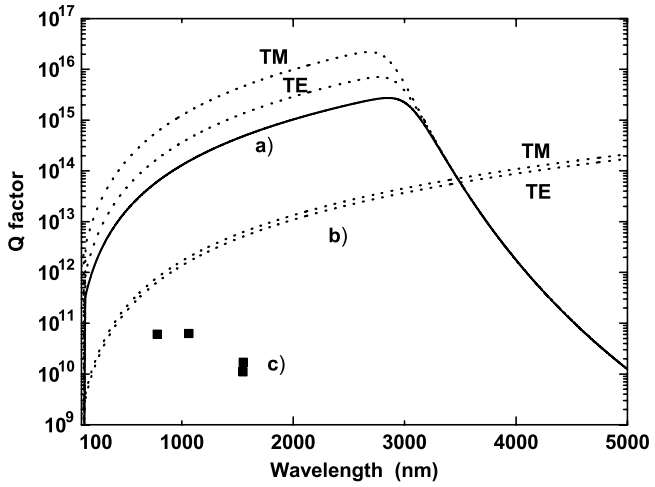

FIG. 9. Maximum intrinsic Q factor of CaF_2 resonator at room temperature. (a) Q factor limited by Rayleigh scattering, multiphonon absorption and electronic absorption in an ideal crystal along with values modified by the geometry of a WGMR for TE and TM modes; (b) surface roughness limited Q factors; (c) experimental data.

sorption wing were estimated from IR absorption data for Corning CaF_2.

In a thorough study it was found [22] that in the best samples of CaF_2 Raman scattering accounts for less than ten percent of the total scattering and thus can be neglected. Stimulated Raman scattering, however, cannot be neglected in our cavities, as will be shown below. Elastic component of Rayleigh scattering in CaF_2 was found to be equal to the bulk Brillouin scattering in a crystal. In a WGM cavity, the acoustic phonon spectrum is modified and Brillouin scattering is further inhibited. In comparison to high-purity fused silica (HPFS), for the best CaF_2 specimens the intrinsic Rayleigh scattering loss is 0.0035, Brillouin loss is 0.005, and extrinsic defect-induced Rayleigh is 0.0015. The total scattering measured in CaF_2 samples at 90 degree is $\alpha(90°)=6\times10^{-4}$ Np/m at 193 nm. This gives a total integrated loss coefficient of $\alpha_r=8\pi\alpha(90°)/3=5\times10^{-3}$ Np/m.

C. Maximum Q factor and its limitations

With the parameters from the two previous sections, we have determined the maximum bulk loss limited Q factor of a CaF_2 WGMR (Fig. 9). Experimental dependence of the refractive index on the wavelength was taken into account. Curve "a" shows what Q factor is possible for an ideal-surface resonator. Electronic absorption is responsible for a sharp decline of the transparency and Q factor for $\lambda < 200$ nm. In the visible and near the IR region, the Q factor is mostly determined by Rayleigh scattering. The decline of Q beyond 3 μm is explained by multiphonon absorption processes. Curve "b" shows that surface scattering would be the main limitation on the Q factor of our cavities if there were no impurities.

The TM modes are closer to the surface, so more scattered light goes back into the modes as compared to the TE modes, giving the higher Q. For the real cavity the TM modes suffer from additional surface scattering and the difference in Q factors is not so pronounced anymore.

IV. DISCUSSION

A. Nonlinear processes in crystalline WGM resonators and optical Q factor

When measuring the optical Q factor, it is important to ensure that nonlinear processes are not present. One way to make sure this is the case is to directly observe the resonant response of a cavity, which for a linear oscillator is known to be described by a Lorentzian lineshape. Deviations from the ideal linear oscillator behavior could serve as a qualitative measure of nonlinearity. In our experiments we found that when the optical power approaches the bistability or the stimulated Raman scattering threshold, the resonator's response is no longer Lorentzian. The Raman lasing threshold is inversely proportional to the square of the Q factor [3], so when ultrahigh Q factors are expected, reducing the optical power used for measurements to low enough levels is a challenge. Thermo-optical oscillatory instability and thermal nonlinearity [23,24] were also observed in the nonlinear regime. Linear resonant curves were only observed in a 5.5 mm cavity at coupled pump power levels of less than 100 nW.

As an example, we measured the cavity response at a pump power of 3 μW. This power was found to be slightly higher than the Raman lasing threshold in our 5.5 mm cavity and is more than an order of magnitude lower than the smallest reported threshold value so far—for an integrated fused silica device [3]. The cavity response at this pump power is strongly non-Lorentzian, with thermo-optical oscillations

also present. Interestingly, the onset of the thermo-optical instability was found to be approximately coincident with the Raman lasing thresholds in large (5 mm) and small (0.1 mm) cavities. Further investigations might show that Raman lasing may be involved in the generation of the oscillations in thermo-optical instability.

Kerr and thermal nonlinearities may explain the departure of the cavity response from the Lorentzian shape, as seen in the Figs. 5 and 6. We may derive the bistability threshold, or the power needed to shift the eigenfrequency of a WGM by its width at half maximum $\Delta f = c/(\lambda Q)$, using a semiclassical approach. Nonlinear index of refraction Δn is given by (see [25])

$$n = n_0 + n_2\langle E^2\rangle = n_0 + \frac{n_2 E_0^2}{2} = n_0 + \Delta n. \tag{8}$$

The shift of the cavity's eigenfrequency f is related to a change in the refractive index,

$$\Delta f = -\frac{\Delta n}{n_0} f. \tag{9}$$

It follows that the change in refractive index that would shift the cavity resonance by its width is

$$\Delta n = \frac{c n_0}{f \lambda Q}. \tag{10}$$

For the energy density created by the K photons stored in a cavity we have

$$\frac{E_0^2 \varepsilon_0 n_0^2}{2} = \frac{K\hbar\omega}{V_{\text{eff}}}, \tag{11}$$

hence, the nonlinear refractive index is

$$\Delta n = \frac{n_2 E_0^2}{2} = \frac{n_2 K \hbar \omega}{V_{\text{eff}} \varepsilon_0 n_0^2}. \tag{12}$$

Combining the expression for the nonlinear part of the refractive index and the required Δn, we obtain K, the number of photons in the cavity sufficient for bistability,

$$K = \frac{V_{\text{eff}} \varepsilon_0 n_0^3}{Q n_2 \hbar \omega}. \tag{13}$$

The intensity buildup factor,

$$\frac{I}{I_0} = \frac{Q\lambda}{\pi^2 a n_0} = \alpha, \tag{14}$$

implies that if we send K/α photons per second to the cavity, the resulting intensity inside the cavity will be equivalent to K photons per second passing each cross section of the WGM. Since each photon completes $\nu_{\text{photon}} = c/(2\pi a n_0)$ round trips around the cavity each second, we need to send

$$\frac{K \nu_{\text{photon}}}{\alpha} = \frac{K\omega}{4Q} = \frac{K}{4\tau} \tag{15}$$

photons per second as an external excitation to have K photons present in the cavity. This flux of photons gives us the bistability threshold power,

$$W_{\text{bist}} = \hbar\omega \frac{\omega}{4Q} \frac{V_{\text{eff}} \varepsilon_0 n_0^3}{Q n_2 \hbar \omega} = \frac{\omega V_{\text{eff}} \varepsilon_0 n_0^3}{4Q^2 n_2}. \tag{16}$$

If one uses the relation for third order susceptibility given in [25], which is valid for a linearly polarized laser beam in isotropic materials and for the beam linearly polarized along [100] axis of a cubic crystal,

$$n_2 = \frac{12\pi\chi^{(3)}_{1111}}{n_0}, \tag{17}$$

and a relation between the systems of units [26]

$$(n_2)_{\text{MKS}} = \tfrac{1}{9} \times 10^{-8} (n_2)_{\text{esu}}, \tag{18}$$

the CGS units formula for bistability threshold is

$$W_{\text{bist}} = \frac{V_{\text{eff}} \omega n_0^4}{192\pi\chi^{(3)} Q^2}. \tag{19}$$

In comparison with the equation (3) in [15], this formula is different by a factor of 1/6 but it gives the values of bistability threshold cited in that paper.

The value of the nonlinear refractive index of CaF_2 is $n_2 = 4.78 \times 10^{-23}$ m^2/V^2 [25–27]. Thus the bistability threshold for 1.5 mm cavity ($V_{ll1} = 2.93 \times 10^{-13}$ m^3, $Q = 4 \times 10^{10}$) is $W_{\text{bist}} = 44$ nW. For a 5 mm cavity with $Q = 6 \times 10^{10}$ the threshold is about 0.2 μW. This shows that a very low input power could shift the eigen-frequency of a crystalline cavity. The fact that the resonant curves presented on Fig. 5 for a pump power of 60 nW are Lorentzian even though the power is 1/3 of the bistability threshold implies that the excited mode was probably not a fundamental WGM, but rather a mode with a large effective volume, $l - m > 1$. For such a mode the bistability threshold is larger than 200 nW and scales with the modal volume, proportional to $\sqrt{2(l-m)+1}$ [see Eq. (6)].

The third order susceptibility associated with the thermal nonlinearity and a specific response time depending on mode configuration may be estimated for TE_{lm1}, TM_{lm1} modes as follows (formula in CGS units from [15]):

$$\chi_T^{(3)} \simeq \frac{n_0 \alpha c \tau_T}{80\pi^2 N k T}, \quad \tau_T = \frac{\lambda^2 l^{2/3} \rho c_p}{\beta n_0^2 \pi^2}. \tag{20}$$

Here α is a bulk attenuation coefficient, k-Boltzmann constant, β-thermal conductivity, and c_p-heat capacity. We have observed that the difference in Q factors for TE and TM modes was much smaller than what might be expected if the Q were limited by scattering. In this case, Q factors would have been proportional to the scattering suppression coefficients $Q_{\text{TE}}/Q_{\text{TM}} \sim K_{\text{TE}}/K_{\text{TM}}$. The demonstrated Q factor of $(6.27 \pm 0.78) \times 10^{10}$ gives a new upper limit on the absorption coefficient in CaF_2 at 1064 nm of $\alpha \simeq 1.4 \times 10^{-4}$ Np/m, derived from Eq. (1). Thus, the given value of α reflects losses in the bulk crystal and the optical Q factor in our cavities is limited by the internal absorption. Using parameters for CaF_2: $\beta = 12$ W/mK, $\rho = 3180$ kg m^{-3}, $c_p = 853$ J/(kg K), $a = 2500$ μm and $\lambda = 1.064$ μm we estimate room temperature

values $\tau_T \simeq 10\ \mu s$ and $\chi_T^{(3)} \simeq 7.3 \times 10^{-12} cm^3/erg = 8.1 \times 10^{-21}\ m^2/V^2$. The concentration of CaF_2 was computed as $N = 2.45 \times 10^{28}\ m^{-3}$. We see that the thermal nonlinearity is dominating in our cavity, which agrees with the experimental observation.

B. Impurities and possibilities for higher Q factors

Measurements of the Q factor at 1550 nm yielded $Q = 1.1 \times 10^{10}$, which is smaller than the previously reported value of $Q = 1.7 \times 10^{10}$ in [4]. This may be explained by the difference in specific fluorite blanks and by the fact that the resonance curve in that work is nonlinear. While theoretical estimates show that the Q factor should increase with the wavelength in the region of experimental measurements (780–1550 nm), we found the opposite to take place, indicating an increase of bulk losses for longer wavelengths (Fig. 9). The development of pure fluorite blanks is mostly driven by the industrial demand for high quality crystals suitable for lithographic lenses transparent in the UV region. Thus one may expect such fluorite blanks to have a reduced amount of impurities absorbing at shorter wavelengths, explaining the lower Q at longer wavelength. For the best fluorite blank from Corning, the total absorption is about an order of magnitude larger than the bulk light scattering [22]. Taking into account the argument from the previous section regarding surface scattering, it follows that the absorption and scattering by impurities is the main loss mechanism in our crystalline WGM cavities.

The crystals used for fabrication of WGMR in this work are the purest available excimer-grade CaF_2 blanks. Nevertheless, these crystals contain significant amounts of atomic impurities such as rare earths and other elements. For a typical excimer grade CaF_2 there may be more than 20 impurities with more than 10 ppb concentration, and the total amount of impurities exceeds 10 ppm, a significant fraction of which is represented by strontium, magnesium, iron, and zinc in the case of our crystals. Strontium was found to improve the radiation resistance of CaF_2 [28]. Ultrahigh Q factors are only possible to achieve at low circulating optical power, where even a minor amount of impurity ions can influence the response of the crystalline medium through resonant Mie-type atomic fluorescence. Unfortunately, information on the absorption spectra of certain ions in CaF_2 lattice is not readily available. The optical properties of impurities are characterized by sharp lines, which correspond to optical transitions. The width of these lines increases with temperature. Thus, one possibility of avoiding the influence of impurities in WGM cavities is to operate them at lower temperatures outside of the spectral regions corresponding to optical transitions of the impurities. According to the analysis presented in Fig. 9, one may expect the Q factor to approach the surface scattering limit of $Q = 10^{12}$ at $\lambda = 1\ \mu m$ if the impurities are "frozen out." If a better surface is fabricated, the material limited Q factor for the available fluorite crystals should approach $Q = 10^{14}$ at $\lambda = 1\ \mu m$ and $Q = 10^{15}$ at $\lambda = 3\ \mu m$ if the impurities are not taken into account. The latter would give an average photon confinement time in excess of one second.

C. Possible applications and conclusion

As the intrinsic optical Q factor of a WGM cavity increases, the power buildup coefficient grows, which in turn lowers the threshold for nonlinear processes. We have shown that by reducing the optical power circulating in an ultrahigh Q crystalline cavity, it is possible to achieve a linear mode and reliably measure the ultrahigh optical Q factors. We have demonstrated values as high as $(6.27 \pm 0.78) \times 10^{10}$ which gives a new upper limit on the absorption coefficient in CaF_2 at 1064 nm of $\alpha \simeq 1.4 \times 10^{-4}$ Np/m. The measured Q factors are the highest values reported for any optical resonator with these dimensions, making crystalline cavities extremely attractive tools in optics. Possible applications of crystalline cavities include compact integrated Raman lasers, cavity QED experiments with crystalline microresonators and quantum nondemolition measurements.

We have shown that Raman lasing was observed in our 5.5 mm cavity at coupled pump power of as low as 3 μW. As the threshold of Raman lasing is inversely proportional to the square of the Q factor, crystalline cavities represent new possibilities for the realization of tunable fiber compatible Raman lasers operating with high efficiency. Another interesting application of high Q crystalline cavities is based on optical parametric oscillations [6]. It might be possible to fabricate an all optical fiber coupled solid state frequency standard based on these devices.

Estimates for a 100 μm $LiNbO_3$ cavity show that a single photon would shift the cavity resonance by as much as 6 Hz. Such a shift can be detected with optical techniques. This then opens up new possibilities for quantum nondemolition (QND) measurements of the number of photons in a cavity. Nevertheless, thermal effects may cause much larger shifts at room temperature [29].

As was discussed in Sec. III A, a number of polishing particles remain attached to the surface of the cavity and if the particles are small enough, the high Q factor is preserved. Observation of these particles suggests the possibility for imprinting quantum dot containing diamond or other nanoparticles into the surface while preserving the Q factor on a very high level, even for the small WGM cavities suitable for cavity QED experiments. In similar experiments with silica microspheres, the application of nanoparticles through deposition usually leads to a significant degradation of the Q factor of the cavity.

The extreme Q factors of crystalline cavities open new opportunities in optical filtering and spectroscopy. A single mode cavity made with lithium niobate could operate as a tunable fiber coupled etalon, more compact and with a higher finesse than a Fabry-Perot cavity. For these applications, resonators with large mode volumes must be selected to reduce the undesirable effects of nonlinearlties.

In conclusion, we have demonstrated measurements of a record high optical Q factor of a fluorite WGMR, fabricated with a diamond grinding technique. We analyzed possible loss mechanisms in crystals and the influence of nonlinear processes. We showed that in order to measure the higher Q factors in linear regime, lower pump power levels must be used to avoid nonlinear processes.

ACKNOWLEDGMENTS

The research has been performed at the Jet Propulsion Laboratory, California Institute of Technology, under a contract with NASA, supported by the DARPA AOSP Program. The authors wish to thank Mark Anderson for taking the AFM images; Ken Evans for SEM images; Andrey Matsko, Makan Mohageg, Anatoliy Savchenkov, and Mikhail Gorodetsky for helpful discussions. We also thank Corning for providing typical impurity content of excimer grade CaF_2.

[1] S. Spillane, T. Kippenberg, K. Vahala, K. Goh, E. Wilcut, and H. Kimble, Phys. Rev. A **71**, 013817 (2005).
[2] S. Goetzinger, O. Benson, and V. Sandoghdar, Appl. Phys. B: Lasers Opt. **73**, 825 (2001).
[3] B. Min, T. Kippenberg, and K. Vahala, Opt. Lett. **28**, 1507 (2003).
[4] A. Savchenkov, V. Ilchenko, A. Matsko, and L. Maleki, Phys. Rev. A **70**, 051804 (2004).
[5] V. Ilchenko, A. Savchenkov, A. Matsko, and L. Maleki, Phys. Rev. Lett. **92**, 043903 (2004).
[6] A. Savchenkov, A. Matsko, D. Strekalov, M. Mohageg, V. Ilchenko, and L. Maleki, Phys. Rev. Lett. **93**, 243905 (2004).
[7] I. Grudinin, A. Matsko, A. Savchenkov, D. Strekalov, V. Ilchenko, and L. Maleki, Opt. Commun. **265**, 33 (2006).
[8] A. Matsko, A. Savchenkov, and L. Maleki, Opt. Lett. **30**, 3066 (2005).
[9] A. Savchenkov, I. Grudinin, A. Matsko, D. Strekalov, M. Mohageg, V. Ilchenko, and L. Maleki, Opt. Lett. **31**, 1313 (2006).
[10] M. Gorodetsky, A. Pryamikov, and V. Ilchenko, J. Opt. Soc. Am. B **17**, 1051 (2000).
[11] D. Vernooy, V. Ilchenko, H. Mabuchi, E. Streed, and H. Kimble, Opt. Lett. **23**, 247 (1998).
[12] M. Lines, J. Appl. Phys. **55**, 4052 (1984).
[13] E. Palik, *Handbook of Optical Constants of Solids* (Academic, New York, 1998).
[14] J. Jackson, *Classical Electrodynamics* (Wiley, New York, 1998), 3rd ed.
[15] V. Braginsky, M. Gorodetsky, and V. Ilchenko, Phys. Lett. A **137**, 393 (1989).
[16] M. Reichling, M. Huisinga, S. Gogoll, and C. Barth, Surf. Sci. **439**, 181 (1999).
[17] M. Lines, Annu. Rev. Mater. Sci. **16**, 113 (1986).
[18] M. Schlesinger, T. Szczurek, M. Wade, and G. Drake, Phys. Rev. B **18**, 6388 (1978).
[19] C. Goerling, U. Leinhos, and K. Mann, Opt. Commun. **249**, 319 (2005).
[20] A. Laufer, J. Pirog, and J. McNesby, J. Opt. Soc. Am. **55**, 64 (1965).
[21] E. Schneider, Phys. Rev. **45**, 152 (1934).
[22] S. Logunov and S. Kuchinsky, J. Appl. Phys. **98**, 053501 (2005).
[23] A. Fomin, M. Gorodetsky, I. Grudinin, and V. Ilchenko, J. Opt. Soc. Am. B **22**, 459 (2005).
[24] T. Johnson, M. Borselli, and O. Painter, Opt. Express **14**, 817 (2006).
[25] M. Weber, ed., *Handbook of Laser Science and Technology*, Vol. 3 (Chemical Rubber Co., Boca Raton, 1986), p. 259.
[26] A. Yariv, *Quantum Electronics* (Wiley, New York, 1975).
[27] R. Adair, L. Chase, and S. Payne, Phys. Rev. B **39**, 3337 (1989).
[28] V. Denks, A. Kotlov, V. Nagirnyi, T. Savikhina, and G. Jones, Phys. Status Solidi A **191**, 628 (2002).
[29] M. Gorodetsky and I. Grudinin, J. Opt. Soc. Am. B **21**, 697 (2004).